ACS OMEGA

http://pubs.acs.org/journal/acsodf

Article

Solar Light-Irradiated Photocatalytic Degradation of Model Dyes and Industrial Dyes by a Magnetic $CoFe_2O_4$–gC_3N_4 S-Scheme Heterojunction Photocatalyst

Debika Gogoi, Priyanka Makkar, and Narendra Nath Ghosh*

Cite This: *ACS Omega* 2021, 6, 4831–4841

Read Online

ACCESS | Metrics & More | Article Recommendations | Supporting Information

ABSTRACT: Magnetic $CoFe_2O_4$–gC_3N_4 nanocomposites were successfully synthesized, and their photocatalytic activities toward the decomposition of model synthetic dyes (e.g., methylene blue, methyl orange, and Congo red) in the presence of H_2O_2 were evaluated under simulated solar light irradiation. The $50CoFe_2O_4$–$50gC_3N_4$ nanocomposite exhibited the highest catalytic activity. The catalytic activity of $50CoFe_2O_4$–$50gC_3N_4$ toward the photodegradation of some industrially used dyes (such as Drimaren Turquoise CL-B p, Drimaren Yellow CL-2R p, and Drimaren Red CL-5B p) was also examined, and the catalyst exhibited its capability to decompose the industrial dyes completely. An aqueous mixture of these dyes was prepared to mimic the dye-containing wastewater, which was fully photodegraded within 30 min. $50CoFe_2O_4$–$50gC_3N_4$ also exhibited facile magnetic separability from the reaction mixture after the accomplishment of photocatalysis reaction and stable performance after five cycles. The high photocatalytic efficiency to degrade several dyes, including dyes used in textile industries, under solar light irradiation makes $50CoFe_2O_4$–$50gC_3N_4$ a promising photocatalyst for the treatment of dye-containing wastewater discharged from industries.

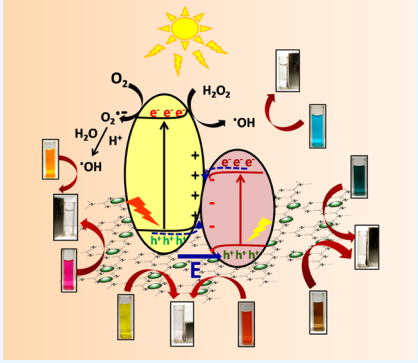

1. INTRODUCTION

A variety of dyes are quite often used by several industries (e.g., textile, paper, plastic, rubber, printing, cosmetics, leather, pharmaceuticals, food processing, etc.) to color their products.[1−4] These industries are causing environmental pollution by discharging dye-containing effluents into the soil and aquatic systems and posing a great threat to the environment. The strong color of the dyes and pigments poses serious esthetic and ecological problems to the acquiring aquatic ecosystem, such as inhibition of benthic photosynthesis.[5] Moreover, some of these dyes are toxic and carcinogenic in nature.[6] To address this issue, scientists and technologists have developed a variety of physical, chemical, and biological techniques to treat the dye-containing effluents.[7−10] Adsorption method, coagulation−flocculation technique, membrane filtration, ion-exchange technique, and so forth are some of the examples of physical processes. Though physical methods are quite often used for wastewater treatment, they are also associated with some limitations. For example, the adsorption process is a slow process and is not very effective for highly colored wastewater. In the case of the membrane separation process, the slow separation rate, the special requirement of filtration, ultrahigh vacuum conditions, and frequent clogging of membrane pores by organic pollutants make this process limited for use in the dye effluent treatment. The generation of a huge amount of sludge is the main disadvantage of coagulation−flocculation-based methods. Another drawback of the physical treatment techniques is that most of the time complete degradation of dyes is not possible. In these processes, although the separation of a pollutant (such as dyes) from water occurs to a large extent, the pollutant is not destroyed/decomposed. As the recovery of dyes from the adsorbents or sludge is not at all cost-effective, the dye molecules are again discharged in the environment in a more concentrated form.[7,11] Hence, biological and chemical treatments of dye-containing wastewater become attractive alternatives. Aerobic treatment, anaerobic treatment, and combined anaerobic−aerobic treatment are the three major types of biological treatment techniques. In these methods, microorganisms play critical roles.[7] The major limitation of the biodegradation processes is that they are not efficient for the dyes having complex aromatic structures. The large-scale application of pure cultures (algal, fungal, and bacterial) is practically limited for wastewater containing various types of dyes because of the dye-specific nature of most of the isolated cultures.[5,12]

Received: November 30, 2020
Accepted: January 27, 2021
Published: February 5, 2021

For the last few years, oxidation process, particularly advanced oxidation process (AOP), to treat wastewater has gained immense attention from scientists.[9,13,14] AOP involves the formation of highly reactive free radicals that oxidize and destroy organic contaminants in a short period. The use of Fenton reagent (H_2O_2−Fe(II)) is a widely used method to treat wastewater that contains dyes exhibiting resistance toward biological treatment or are poisonous to live biomass.[15,16] However, the generation of excessive sludge and short life of some of the oxidizing agents (e.g., O_3), which generate radicals, are the disadvantages of this process.[13]

Recently, the UV light-assisted oxidation process has become an attractive approach. Here, UV radiation activates chemicals (e.g., H_2O_2) and produces free radicals. These free radicals degrade the dye molecules to CO_2 and H_2O. Several wide band gap semiconductors (such as TiO_2, ZnO, etc.) have been examined for the photocatalytic degradation of dyes.[17,18] In this aspect, TiO_2 is one of the most widely explored semiconductors by several researchers.[17,19−22] However, the photocatalytic activity of TiO_2 is limited to UV or near-UV radiation (≤380 nm) because of its wide band gap (3.2 eV).[23−26] The large-scale application of usage of UV radiation is limited because it makes the process costly and non-ecofriendly. Therefore, the current research is concentrated on the development of such photocatalysts for wastewater treatment, which can efficiently degrade dyes under solar light irradiation.[27−31] Tuning the band gap of the photocatalyst, so that it can be activated under visible or solar light irradiation, is a viable solution. To achieve such photocatalysts, synthesizing nanocomposites by combining two semiconducting nanoparticles having matching band gaps is an interesting strategy adopted by several researchers.[32−39] Our previous study showed that reduced graphene oxide (rGO)-$CoFe_2O_4$ nanocomposites can exhibit photocatalytic activity toward the degradation of some dyes under visible light irradiation. However, the synthesis of rGO via preparation of graphene oxide by the Hummers method, followed by its reduction to rGO, is a cumbersome, environment-unfavorable, and time-consuming method. Therefore, we have aimed to develop a photocatalyst that is capable of photodegrading different types of dyes (model dyes as well as industrially used dyes) under solar light and at the same time can be synthesized by a simple but environment-friendly method as well as can be separated from the reaction mixture easily.

In the present study, we have designed a photocatalyst composed of graphitic carbon nitride (gC_3N_4) and $CoFe_2O_4$ (CF) nanoparticles to degrade several dyes under visible light irradiation. Here, we have chosen gC_3N_4 as one of the components of the nanocomposite because the advantages it offers are low cost, easy preparation protocol, nontoxicity, ability to adsorb organic molecules via $\pi-\pi$ interaction, and so forth. However, gC_3N_4 suffers from a high recombination rate of the photogenerated electron−hole,[37,40] low conductivity, low specific surface area,[41] insignificant absorption above 460 nm in solar spectra, and so forth.[42] These factors limit the wide application of gC_3N_4 as the photocatalyst. Designing a nanocomposite composed of gC_3N_4 with another semiconductor having a matching band gap is an attractive solution to tune the band gap and to address the limitation associated with gC_3N_4. Examples of such nanocomposites are ZnO/gC_3N_4,[43] TiO_2/gC_3N_4,[44] SnO_2/gC_3N_4,[45] WO_3/gC_3N_4,[46] and so forth.

We have chosen $CoFe_2O_4$, which is a low band gap semiconductor (band gap ∼ 1.08 eV),[47,48] as another component of the photocatalyst. Though $CoFe_2O_4$ does not exhibit an appreciable photocatalytic activity toward dye degradation,[49] it can suppress the electron−hole recombination of gC_3N_4 by forming a heterojunction when coupled with gC_3N_4. By varying the composition of gC_3N_4 and CF, the band gap energy of the nanocomposite can be tuned in such a way that it can act as a photocatalyst in the visible light region. Moreover, as CF is magnetic in nature (saturation magnetization = 75 emu/g),[50] its presence in the nanocomposite makes the photocatalyst a magnetically separable catalyst. This feature of this catalyst solves the separation-related problem of the general nanosized catalysts.

A very few reports are available on the synthesis of the gC_3N_4−$CoFe_2O_4$ composite and the study of its photocatalytic activity toward the degradation of dyes. Recently, Hassani et al. have reported the synthesis of mesoporous gC_3N_4−$CoFe_2O_4$ composite and its ability to photodegrade Malachite green dye under UV radiation.[41] This catalyst exhibited the maximum degradation efficiency of 93.41% in a reaction time of 120 min. They have also studied the photodegradation of methylene blue, acid orange 7, and rhodamine B. They have also reported the sonocatalytic activity of mesoporous gC_3N_4−$CoFe_2O_4$ toward the removal of methylene blue.[51] Huang et al. have synthesized the $CoFe_2O_4$−gC_3N_4 nanocomposite and showed that this photocatalyst can degrade 97.3% of methylene blue dye under visible light irradiation within 3 h.[49] Inbaraj et al. have synthesized the $CoFe_2O_4$−gC_3N_4 nanocomposite by employing the sol−gel autocombustion method and hydrothermal method and reported that the synthesized nanocomposite exhibited 98% of photodecomposition of methylene blue under solar light irradiation within 150 min.[52] Yao et al. have reported the synthesis of the $CoFe_2O_4$−gC_3N_4 catalyst and demonstrated its photo-Fenton-like photocatalysis for organic dyes.[53] To the best of our knowledge, till date, the application of the CF−gC_3N_4 nanocomposite as a photocatalyst to degrade various types of dyes, particularly industrially used dyes, has not yet been well explored.

We have synthesized nanocomposites composed of varying amounts of $CoFe_2O_4$ and gC_3N_4. The synthesized materials (i.e., pure CF, pure gC_3N_4, and CF−gC_3N_4 nanocomposites) were characterized by using X-ray diffraction (XRD), thermogravimetric analysis (TGA), FT-IR spectroscopy, Raman spectroscopy, UV−vis diffuse reflectance spectroscopy (UV-DRS), field emission scanning electron spectroscopy (FESEM), and energy-dispersive X-ray spectrometry (EDXS). We have determined the change of band gap energy of the synthesized nanocomposites with the variation of their compositions. To evaluate the photocatalytic activity of the synthesized nanocomposites, we have performed the photodegradation reaction of different dye solutions in the presence of H_2O_2 under simulated solar light irradiation with a light intensity of 10000 lux (measured by using a light meter (LX-101A). Initially, the photocatalytic degradation of different model dyes [such as methylene blue (MB), methyl orange (MO), Congo red (CR), and a mixture of these dyes] was investigated, and the optimum composition of the nanocomposite which can exhibit the highest photocatalytic efficiency was determined. Then, the photocatalytic activity of this catalyst was also tested for the industrially used dyes [such as Drimaren Turquoise CL-B p (Turq CL-B), Drimaren Yellow CL-2R p (Yell CL-2R), and Drimaren Red CL-5B p

https://dx.doi.org/10.1021/acsomega.0c05809
ACS Omega 2021, 6, 4831−4841

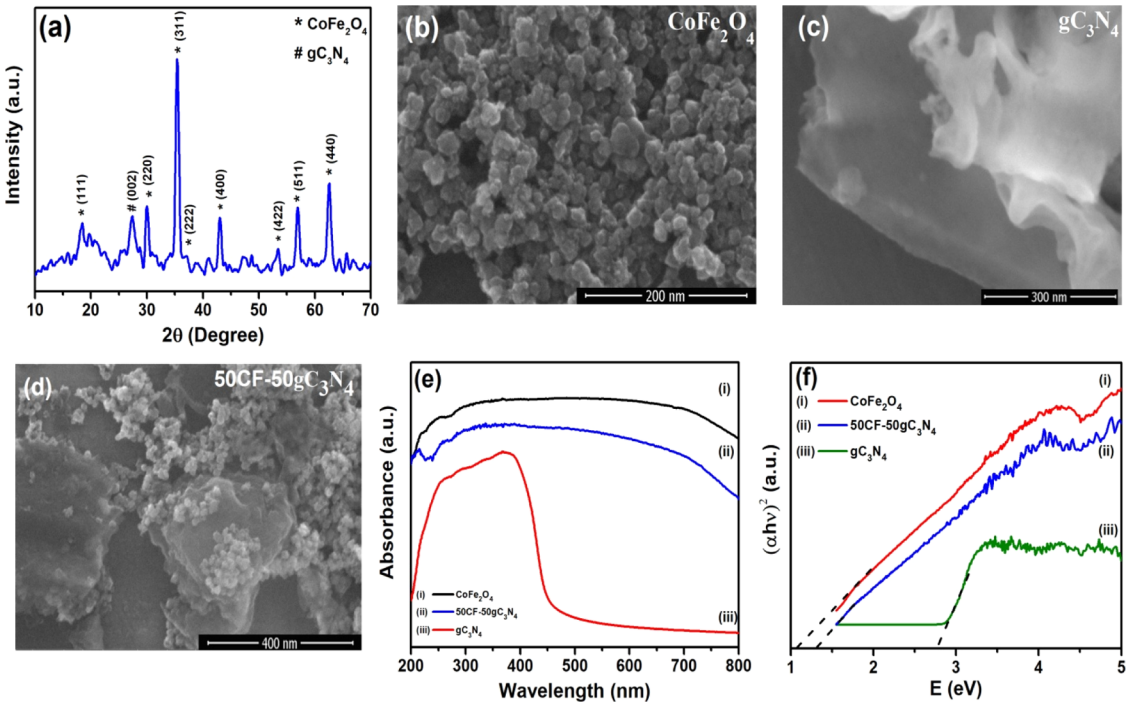

Figure 1. (a) XRD patterns of the 50CF−50gC_3N_4 nanocomposite, (b−d) FESEM micrographs, (e) UV−vis absorption spectra, (f) $(\alpha h\nu)^2$ versus photon energy plots of pure $CoFe_2O_4$, pure gC_3N_4, and 50CF−50gC_3N_4 nanocomposite.

(Red CL-5B)], which are widely used in textile industries. To mimic the dye-containing wastewater, we have prepared an aqueous mixture of these industrial dyes and performed the photocatalysis reaction. The synthesized catalyst exhibited excellent photocatalytic activity toward the degradation of model dyes as well as industrial dyes. After the first cycle of catalysis reaction, the catalyst was magnetically recovered, and the efficiency of the recovered catalyst was tested for a couple of cycles.

2. RESULTS AND DISCUSSION

2.1. Structure and Morphology of the CF−gC_3N_4 Nanocomposites. The XRD patterns of the synthesized materials (e.g., pure gC_3N_4, CF, and CF−gC_3N_4 nanocomposites) are presented in Figures S1−S3. In the XRD pattern of the pure CF sample, the diffraction peaks at 2θ = 18.2, 30.1, 35.5, 37.1, 43.1, 53.4, 56.9, and 62.6°, corresponding to the (111), (220), (311), (222), (400), (422), (511), and (440) diffraction planes [JCPDS card no 22-1086], are observed.[48,54] The XRD pattern of pure gC_3N_4 displays two peaks at 2θ = 13.1 and 27.3°, which can be indexed as (100) and (002) planes, respectively. These peaks indicate the in-plane structural packing motifs of tri-*s*-triazine units and the interlayer stacking of the conjugated aromatic system of gC_3N_4.[55,56] In the XRD pattern of CF−gC_3N_4 nanocomposites, all the diffraction peaks of CF and gC_3N_4 are observed, but in some cases (where the gC_3N_4 amount is less) the diffraction peaks characteristic of gC_3N_4 are not present. This could be because of the too thin (nanometer scale) nature of gC_3N_4 layers.[33,57−59] As a representative, the XRD pattern of 50$CoFe_2O_4$−50gC_3N_4 is shown in Figure 1a, which displays both the characteristic peaks of CF and gC_3N_4.

We have investigated the microstructures of the synthesized pure gC_3N_4, pure CF, and CF−gC_3N_4 nanocomposites by FESEM. Figure 1b shows the agglomeration of almost spherical CF nanoparticles (with an average particle size of ∼20−25 nm). Figure 1c displays the nanometer-thin sheets of gC_3N_4. Figure 1d displays the FESEM image of the 50CF−50gC_3N_4 nanocomposite, depicting the dispersion of CF nanoparticles on the surface of the gC_3N_4 sheet. The EDS spectra (Figure S4) shows the presence of peaks for C, N, Co, Fe, and O in this nanocomposite.

Figure S5 presents the FT-IR spectra of pure gC_3N_4, CF, and CF−gC_3N_4 nanocomposites. In the FT-IR spectrum of gC_3N_4, the prominent peaks are present at (i) 1636 cm^{-1} for C═N stretching vibration, (ii) 1563 and 1411 cm^{-1} characteristic to the s-triazine ring vibrations, (iii) 1326 and 1246 cm^{-1} for C−N stretching, and (iv) 809 cm^{-1} due to the s-triazine ring vibration.[60−62] The FT-IR spectrum of CF shows a peak at 591 cm^{-1}, which corresponds to the lattice absorption of M−O (where M = Fe^{3+}, Co^{2+}).[63] In the FT-IR spectra of CF−gC_3N_4 nanocomposites, all the characteristic peaks of gC_3N_4 and CF are observed.

Figure S6 shows the Raman spectra of pure CF, pure gC_3N_4, and 50CF−50gC_3N_4. In the Raman spectra of pure gC_3N_4, the Raman peaks are present at 461, 570, 688, 745, 962, 1253, 1406, 1464, 1559, and 1616 cm^{-1}, which can be attributed to the layer−layer deformation vibrations or the correlation vibrations, out-of-plane bending mode of the graphitic domain, breathing mode of the s-triazine ring, lattice vibration of gC_3N_4, D band, G band, and vibration modes of CN heterocycles, respectively.[64−68] The Raman spectra of pure CF displays the T_{2g} and A_{1g} modes at 460 and 672 cm^{-1}, corresponding to the vibrational modes of octahedral iron and tetrahedral cobalt, respectively, present in CF.[69] The presence of Raman bands corresponding to both CF and gC_3N_4 in the Raman spectra of the synthesized nanocomposite also confirms their presence in the 50CF−50gC_3N_4 nanocomposite.

XRD, FESEM, IR spectroscopy, and Raman spectral analysis clearly indicate the formation of pure CF nanoparticles on the

https://dx.doi.org/10.1021/acsomega.0c05809
ACS Omega 2021, 6, 4831−4841

surface of gC_3N_4 sheets. The chemical reactions involved in the synthesis of $CoFe_2O_4$ can be presented by the following equations[48]

$$Co^{2+} + 2OH^- \rightarrow Co(OH)_2 \quad (1)$$

$$Fe^{3+} + 3OH^- \rightarrow FeO(OH)_3 \quad (2)$$

$$2\,FeO(OH)_3 + Co(OH)_2 \xrightarrow[16\,h]{160\,^\circ C} CoFe_2O_4 + 2H_2O \quad (3)$$

To estimate the amount of gC_3N_4 present in the CF−gC_3N_4 nanocomposites, we have performed TGA of pure CF, pure gC_3N_4, and CF−gC_3N_4 nanocomposites in the temperature range of 30−800 °C (Figure S7). Pure CF shows its thermal stability in this temperature range. For pure gC_3N_4, the decomposition starts at ∼400 °C, and 100% decomposition completes at 700 °C. TGA of CF−gC_3N_4 nanocomposites was performed to calculate the amount of undecomposed sample after 700 °C. This remaining amount of solid indicates the amount of CF present in the composite. TGA thermograms of the nanocomposites show that the weight % of CF and gC_3N_4 matches well with the composition, which is expected as per the synthesis of the samples. For example, in the case of the 50CF−50gC_3N_4 composite, ∼50% solid (i.e., CF) remains undecomposed above 600 °C, indicating the presence of 50 wt % CF and 50 wt % gC_3N_4 in this nanocomposite.

2.2. Optical Properties of the CF−gC_3N_4 Nanocomposites. We have studied the optical absorption properties of the as-synthesized materials by using UV−vis diffuse reflectance spectroscopy. Figure 1e represents the UV−vis DRS spectra of pure CF, pure gC_3N_4, and 50CF−50gC_3N_4 nanocomposite. Pure gC_3N_4 shows an absorption edge at ∼460 nm, and pure CF displays a broad absorption range from 200 to 800 nm. In the case of CF−gC_3N_4 nanocomposites, the red shift of the absorption edge position was observed compared to pristine gC_3N_4, and the absorption of visible light enhances to a great extent with the increasing CF weight % in the nanocomposite (Figure S8). This observation is similar to the results reported by several researchers.[35,36,42,49,53,70,71] This property of the nanocomposites can be exploited for their application as photocatalysts, which can be activated upon visible light irradiation. The band gap energy (E_g) of the synthesized materials was calculated from the $(\alpha h\nu)^2$ versus photon energy plot (Figure 1f) by using the Kubelka−Munk equation[72]

$$\alpha h\nu = A(h\nu - E_g)^{n/2} \quad (4)$$

where h, ν, and E_g are Planck's constant, frequency of light, and band gap, respectively. The band gap values of the synthesized pristine gC_3N_4 and pure CF nanoparticles are 2.76 and 1.04 eV, respectively. For the nanocomposites, the band gap value is increased with the increasing gC_3N_4 content, and the band gap values increase from 1.11 to 1.31 eV when the weight % of gC_3N_4 is increased from 5 to 50 wt %. This is mainly owing to the synergistic effect arising from the formation of heterojunctions between the CF nanoparticles and gC_3N_4 in the nanocomposite, which causes an easy electron transfer between these two components. This observation is in agreement with the other substantive findings in the literature.[36,42,49,70,71]

2.3. Photocatalytic Activity of CF−gC_3N_4 Nanocomposites. To evaluate the photocatalytic activity of the synthesized nanocomposites, we have performed the photodegradation reaction of different dye solutions under visible light irradiation (emitted from the solar light simulator) in the presence of H_2O_2. Initially, we used several model synthetic dyes (e.g., MB, MO, and CR) to determine the optimum composition of the nanocomposites which can exhibit the highest catalytic activity. Then, we conducted the photocatalytic reaction toward the degradation of some of the industrially used dyes (e.g., Turq CL-B, Yell CL-2R, and Red CL-5B) to demonstrate the potential use of the synthesized nanocomposite as an effective photocatalyst to treat the dye-containing wastewater discharged from industries.

Of all the dyes, pure CF showed a poor photocatalytic activity. The highest efficiency of the photocatalyst is observed when the catalyst contained 50 wt % CF and 50 wt % gC_3N_4 (50CF−50gC_3N_4). For MB, after 3 h of exposure to light, pure CF- and pure gC_3N_4-catalyzed reactions showed ∼49 and ∼63% of dye degradation, respectively. With the increasing weight % of gC_3N_4 in the nanocomposite, the performance of the nanocomposite as photocatalyst has increased. For example, in the case of 95CF−5gC_3N_4, 83% photodegradation of MB has occurred after 3 h of reaction, whereas 50CF−50gC_3N_4 showed ∼100% MB degradation in 45 min. A similar trend has been observed for the photocatalysis reaction of other dyes. The photocatalyst that composed of 50 wt % CF and 50 wt % gC_3N_4 (50CF−50gC_3N_4) displayed the highest efficiency toward the degradation of dyes. The change of photocatalytic efficiency (i.e., % of dye degradation at different reaction times) with varying compositions of the photocatalyst is tabulated in Table 1 and depicted in Figures 2 and S9−S11.

Table 1. Photocatalytic Activity of CF−gC_3N_4 Nanocomposites toward the Decomposition of Different Dyes

	% of degradation (time)		
catalyst	MB	MO	CR
pure CF	49% (3 h)	59% (3 h)	69% (2.5 h)
pure gC_3N_4	63% (3 h)	100% (2.5 h)	93% (2 h)
95CF−5gC_3N_4	83% (3 h)	76% (3 h)	75% (2.5 h)
90CF−10gC_3N_4	87% (3 h)	81% (3 h)	86% (2.5 h)
85CF−15gC_3N_4	98% (3 h)	87.7% (3 h)	89% (2.5 h)
75CF−25gC_3N_4	∼100% (1.5 h)	93% (2 h)	95% (2 h)
50CF−50gC_3N_4	∼100% (45 min)	∼100% (1.5 h)	∼100% (1.5 h)

Figure 2a−c shows the UV−vis spectra displaying the decrease of the intensity of λ_{max} with increasing reaction times for MB, MO, and CR, respectively, for the 50CF−50gC_3N_4-catalyzed photodegradation reaction. Figure 2d−f displays the variation of C_t/C_0 ratio for MB, MO, and CR with the progress of reaction time when photocatalytic reactions are performed in the presence of a catalyst (pure CF, gC_3N_4, and 50CF−50gC_3N_4). Upon photocatalysis, the total organic carbon (TOC) removal ratio for MB, MO, and CR solutions is 69, 36, and 78.11%, respectively. We have also performed the 50CF−50gC_3N_4-catalyzed photocatalysis reaction with an aqueous solution containing a mixture of MB, MO, and CR dyes (60 ppm). The complete photocatalytic decomposition of this dye mixture occurred in 3 h (Figure 2g). We have observed that the photocatalytic activity of 50CF−50gC_3N_4 is better than that of the rGO-$CoFe_2O_4$ nanocomposites, which we have investigated in our previous study.[48]

Now, to examine whether 50CF−50gC_3N_4 can be used to treat dye-containing industrial wastewater, we performed the photocatalysis reaction using three different dyes (e.g., Turq

https://dx.doi.org/10.1021/acsomega.0c05809
ACS Omega 2021, 6, 4831−4841

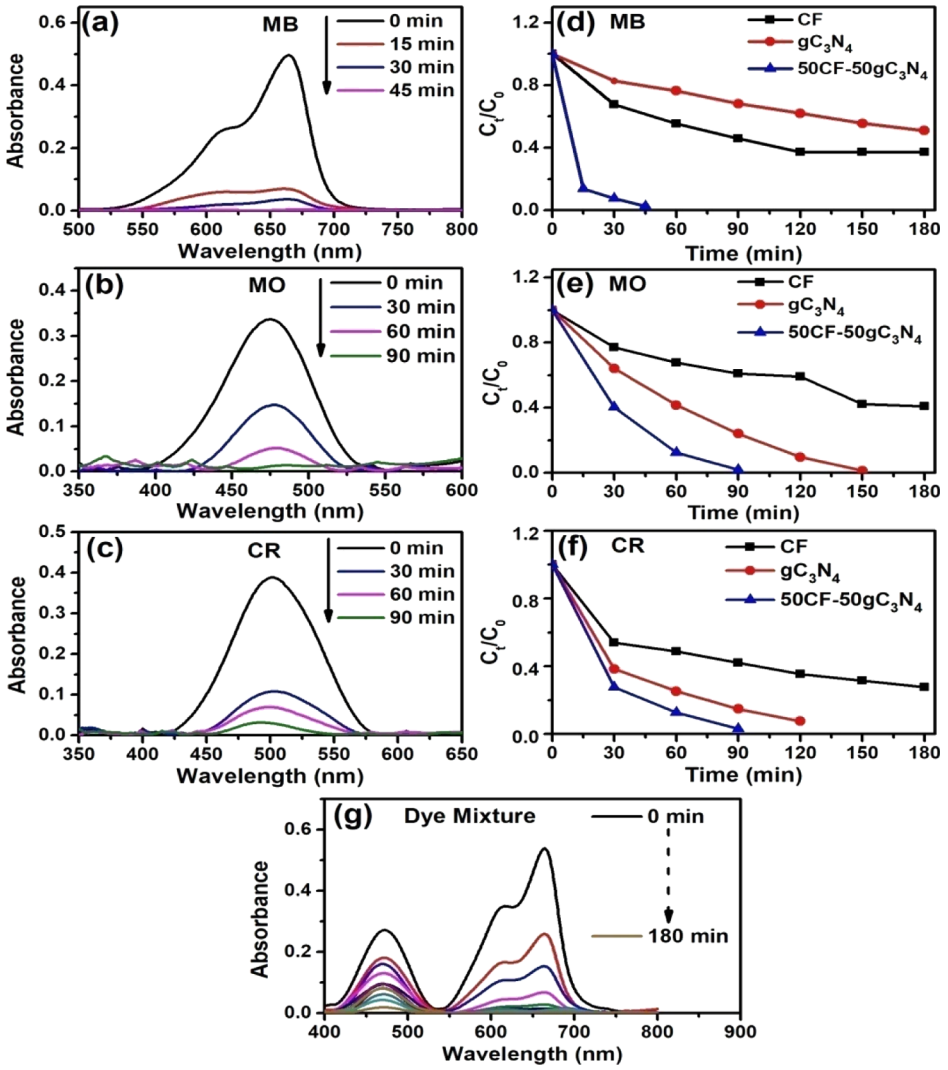

Figure 2. (a–c) Time-dependent UV–vis spectral changes of the 50CF–50gC_3N_4-catalyzed photodecomposition reaction of different dyes (MB, MO, and CR). (d–f) Photodegradation rates of different dyes catalyzed by gC_3N_4, CF, and 50CF–50gC_3N_4. (g) Time-dependent UV–vis spectral changes of the 50CF–50gC_3N_4-catalyzed photodecomposition reaction of the model dye mixture.

CL-B, Yell CL-2R, and Red CL-5B), which are widely used in textile industries and present in the wastewater discharged from these industries. Here also, it is observed that 50CF–50gC_3N_4 exhibited a better photocatalytic activity than pure CF and pure gC_3N_4 (Figure 3d–f). In the presence of 50CF–50gC_3N_4, the time required for 100% decomposition of Turq CL-B, Yell CL-2R, and Red CL-5B is 90, 45, and 60 min, respectively. To mimic the industrial wastewater, we have prepared an aqueous mixture of these three dyes, and the complete photodegradation of this dye mixture occurred within 30 min when catalyzed by 50CF–50gC_3N_4 (Figure 3g). In this case, the TOC removal ratio is 66.74%.

2.4. Photocatalytic Reaction Mechanism. To understand the role of H_2O_2 and the 50CF–50gC_3N_4 catalyst in the photodecomposition reaction of MB, we have performed the experiment in the presence of only H_2O_2 (but no catalyst) and only with the catalyst (but no H_2O_2). In both cases, the reaction is found to be significantly slower. After 45 min of reaction time, only 17% decomposition occurred when only H_2O_2 is present. Similarly, when only the catalyst (50CF–50gC_3N_4) is present, 35% degradation of MB occurred after 45 min. However, when both H_2O_2 and 50CF–50gC_3N_4 are present in the reaction mixture, 100% degradation of MB is achieved in 45 min (Figure 4). These experiments confirmed that the activation of H_2O_2 was promoted by the catalyst when excited by visible light. As discussed before, the % of degradation of dyes is appreciably higher when the photocatalysis reaction is catalyzed by the 50CF–50gC_3N_4 nanocomposite in comparison with pure CF- or pure gC_3N_4-catalyzed reaction (Figure 2d). This enhancement of the catalytic activity of the 50CF–50gC_3N_4 nanocomposite can be attributed to the synergistic effect arising from the coupling of CF and gC_3N_4 in the nanocomposite.

The CF–gC_3N_4-catalyzed photocatalytic reaction proceeds via the step-scheme (S-scheme) heterojunction mechanism, as described by Xu et al., and is presented in Scheme 1.[73] In the S-scheme heterojunction mechanism, heterojunctions are formed at the interface between two photocatalysts having a staggered band structure. These heterojunctions can increase the usage of photoinduced charge carriers to generate an enormous amount of active species.[74−77] The conduction (CB) and valence band (VB) values of CF are +0.91 and +1.71 eV, whereas those for gC_3N_4 are −1.13 and +1.57 eV, respectively.[49] Under visible light irradiation, both CF and

https://dx.doi.org/10.1021/acsomega.0c05809
ACS Omega 2021, 6, 4831−4841

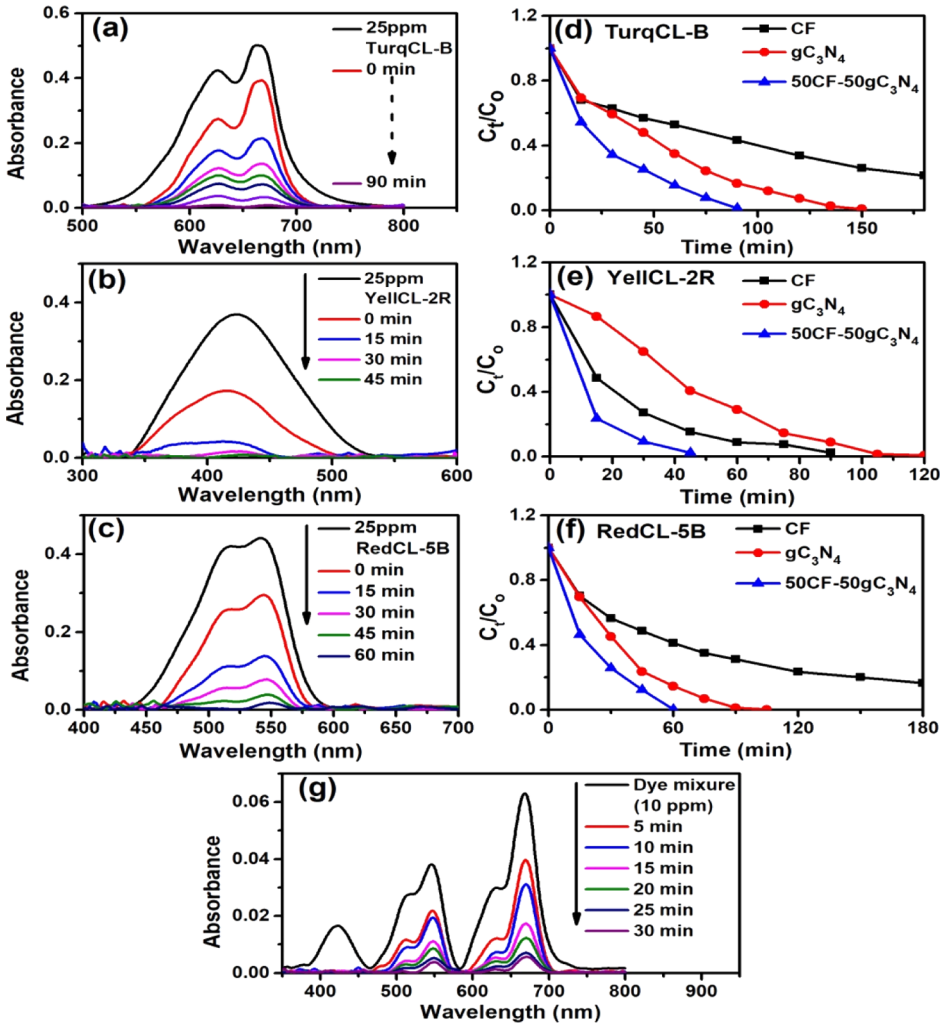

Figure 3. (a–c) Time-dependent UV–vis spectral changes of the 50CF–50gC_3N_4-catalyzed photodecomposition reaction of industrial dyes (Turq CL-B, Yell CL-2R, and Red CL-5B). (d–f) Photodegradation rates of the dyes catalyzed by gC_3N_4, CF, and 50CF–50gC_3N_4. (g) Time-dependent UV–vis spectral changes of the 50CF–50gC_3N_4-catalyzed photodecomposition reaction of the industrial dye mixture.

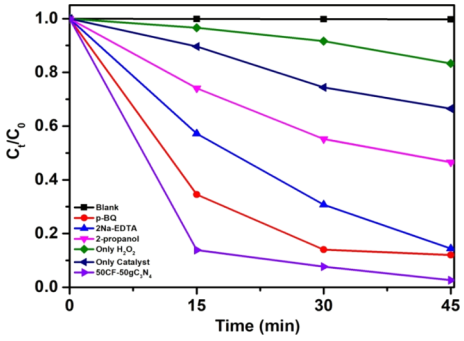

Figure 4. Effect of different radical scavengers on the photodegradation reaction of MB.

gC_3N_4 became excited, which leads to the formation of photogenerated holes and electrons in their VB and CB, respectively. The powerful photogenerated electrons and holes are reserved in the CB of gC_3N_4 and VB of CF, respectively, and the pointless charge carriers recombine and introduce a redox potential. When CF and gC_3N_4 come in contact, the electrons of gC_3N_4 diffuse into CF, and in the contact interface, an electron depletion layer and electron accumulation layer form. This electric field helps in the transfer of photogenerated electrons from CF to gC_3N_4. In the contact interface between CF and gC_3N_4, their individual Fermi energies (E_f) align to the same level, which causes band bending and results in the recombination of electrons in the CB of CF and holes in the VB of gC_3N_4. Moreover, because of the Coulombic attraction, the photogenerated electrons in the CB of CF and holes in the VB of gC_3N_4 also recombine. Thus, the useless electrons and holes recombine, whereas the powerful photogenerated electrons in the CB of gC_3N_4 and holes in the VB of CF are retained to proceed the photocatalysis reaction. During the photocatalysis reaction, these powerful photogenerated electrons and holes produce superoxide radicals ($O_2^{\bullet -}$) and hydroxyl radicals ($^{\bullet}OH$), and these radicals degrade the dye molecules. The photocatalytic reactions which are involved in this dye degradation process can be presented in eqs 5–9.

To understand the role of these reactive species, we have performed a series of radical tapping experiments by using *p*-benzoquinone (BQ), EDTA-2Na, and isopropanol (IPA) which act as scavengers for $O_2^{\bullet -}$, holes, and $^{\bullet}OH$ respectively.[33,37,49,78] Figure 4 shows that the % decomposition of MB was slightly decreased with the addition of BQ and EDTA-2Na. It is observed that after 45 min of reaction, ~88

https://dx.doi.org/10.1021/acsomega.0c05809
ACS Omega 2021, 6, 4831–4841

Scheme 1. Proposed S-Scheme Mechanism of the Degradation of Dyes by CF−gC_3N_4 Nanocomposites

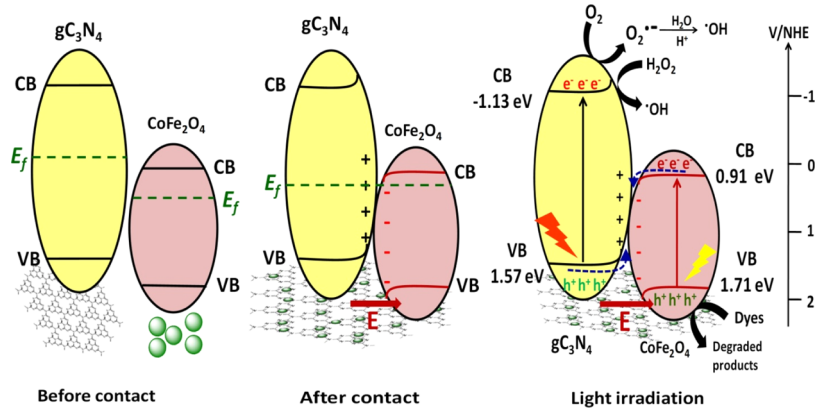

and ∼86% decomposition of MB occurred in the presence of BQ and EDTA-2Na, respectively. However, ∼100% photodegradation of MB occurred when no scavenger was present. The rate of MB degradation became significantly slow in the presence of IPA, and only 55% of MB is decomposed within 45 min. These results indicate that $^{\bullet}OH$ plays a more critical role than holes and $O_2^{\bullet-}$.

$$CF - gC_3N_4 \xrightarrow{h\nu} CF(e^-\text{---}h^+) - gC_3N_4(e^-\text{---}h^+) \quad (5)$$

$$O_2 + e^- \rightarrow O_2^{\bullet-} \quad (6)$$

$$O_2^{\bullet-} + H_2O \xrightarrow{+H^+} 3^{\bullet}OH \quad (7)$$

$$H_2O_2 + e^- \rightarrow {}^{\bullet}OH + {}^{-}OH \quad (8)$$

$$^{\bullet}OH + \text{dye} \rightarrow \text{degradation product} \quad (9)$$

3. REUSABILITY

After the photocatalysis reaction, the catalyst was magnetically separated from the reaction mixture and used for the next cycle. Figure 5a,b shows the complete decolorization of the dyes because of photodegradation and the separation of the 50CF−50gC_3N_4 catalyst by a magnet. We have observed that the catalyst retains its efficiency for the first three cycles, after

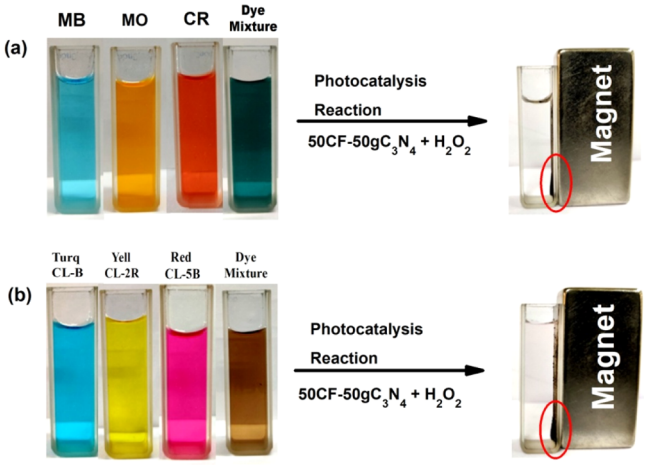

Figure 5. (a) Decolorization of model dyes by the photocatalysis reaction; (b) decolorization of industrial dyes by the photocatalysis reaction, and separation of the catalyst by using a magnet.

which it slightly decreases (Figure 6). The XRD and FESEM investigations of the recycled catalyst reveal that no significant

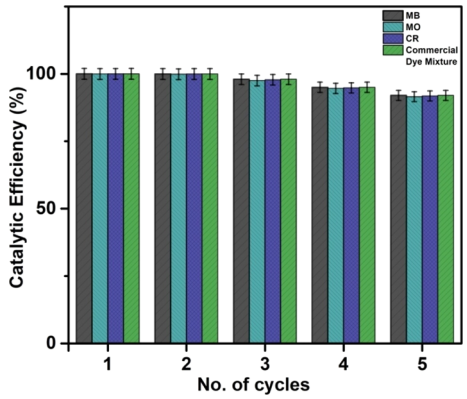

Figure 6. Reusability of the catalyst 50CF−50gC_3N_4 toward the photodegradation of MB, MO, CR, and the industrial dye mixture.

change in the crystal structure and morphology of the catalyst occurred during the photocatalysis reaction (Figure S12).

4. CONCLUSIONS

We have successfully synthesized $CoFe_2O_4$−gC_3N_4 nanocomposites. These nanocomposites exhibit strong absorption in the visible light region, and their band gap can be tuned simply by varying the amount of $CoFe_2O_4$ and gC_3N_4 in the nanocomposite. Among these nanocomposites, 50$CoFe_2O_4$−50gC_3N_4 shows the highest photocatalytic activity for the degradation of several model dyes (e.g., MB, MO, and CR) as well as industrially used dyes (such as Turq CL-B, Yell CL-2R, and Red CL-5B) and a mixture of dyes. The photocatalytic activities of 50CF−50gC_3N_4 for the degradation of dyes are significantly higher than those of individual $CoFe_2O_4$ and gC_3N_4. This enhancement could be due to the synergistic effect arising from the intimate coexistence of $CoFe_2O_4$ and gC_3N_4 in the catalysts and their staggered band structure. The photocatalytic efficiency of 50$CoFe_2O_4$−50gC_3N_4 is comparable and in some cases superior to that of many reported photocatalysts (Table S1).[33,40,71,79−87] Moreover, the capability of this catalyst to degrade a variety of dyes, particularly industrially used dyes under solar light irradiation, makes it an attractive photocatalyst. This photocatalyst also offers easy magnetic separation and shows a stable catalytic efficiency even after five cycles. 50$CoFe_2O_4$−50gC_3N_4 demonstrates its

https://dx.doi.org/10.1021/acsomega.0c05809
ACS Omega 2021, 6, 4831−4841

Scheme 2. Synthetic Route of CF−gC_3N_4 Nanocomposites

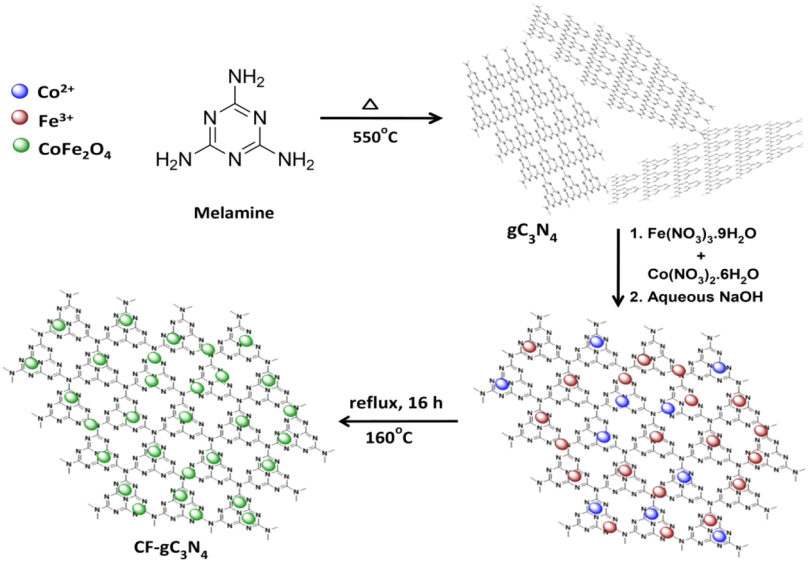

potential as an efficient photocatalyst for the wastewater treatment of dye-containing effluents discharged from industries.

5. EXPERIMENTAL SECTION

5.1. Synthesis of $CoFe_2O_4$−gC_3N_4 Nanocomposites. The nanocomposites composed of $CoFe_2O_4$ and gC_3N_4 were synthesized by employing a two-step process. The schematic presentation of this synthetic methodology is depicted in Scheme 2. In the first step, gC_3N_4 powder was prepared by the thermal treatment of melamine at 550 °C for 2 h at a heating rate of 5 °C/min.[34] In a beaker, a dispersion of gC_3N_4 in an aqueous medium was prepared by adding a calculated amount of gC_3N_4 in water, followed by ultrasonication. In the next step, in this aqueous dispersion of gC_3N_4, a mixture of $Co(NO_3)_2{\cdot}6H_2O$ and $Fe(NO_3)_3{\cdot}9H_2O$ (molar ratio 1:2) in the polyethylene glycol and water medium (weight ratio 1: 5) was added. In this mixture, an aqueous solution of NaOH (2 M) was added dropwise till the pH reached ∼11. This mixture was refluxed at 160 °C for 16 h. After reflux, the reaction mixture was allowed to cool down to room temperature. The black-colored product thus formed was magnetically separated from the reaction mixture by applying a permanent magnet externally. After separation, this solid powder was washed with water, ethanol, and finally with acetone and then dried at 60 °C for 10 h. Using this protocol, nanocomposites having various weight % of gC_3N_4 and CF nanoparticles were synthesized by varying the amount of gC_3N_4, $Co(NO_3)_2{\cdot}6H_2O$, and $Fe(NO_3)_3{\cdot}9H_2O$. The nanocomposites having 5, 10, 15, 25, and 50 wt % gC_3N_4 content are referred as 95CF−5gC_3N_4, 90CF−10gC_3N_4, 85CF−15gC_3N_4, 75CF−25gC_3N_4, and 50CF−50gC_3N_4, respectively. Pure CF nanoparticles were also synthesized by employing the same protocol, except that gC_3N_4 was not added to the reaction mixture.

5.2. Photocatalytic Activity Measurement. To evaluate the photocatalytic activity of the synthesized materials, photodegradation reactions of different dye solutions in the presence of H_2O_2 under simulated solar light irradiation was performed. Initially, the photocatalytic degradation of different model dyes (such as MB, MO, CR) was investigated.

First, aqueous solutions of MB (25 ppm), CR (25 ppm), and MO (10 ppm) were prepared. In a typical photocatalysis reaction, 50 mL of dye solution was taken in a beaker and mixed with 25 mg of catalyst (50 mg in the case of MO). This mixture was stirred in the dark for 30 min to reach the absorption−desorption equilibrium between the catalyst and dye solution. The UV−vis spectra of the mixture were recorded before and after the stirring of the reaction mixture in the dark. It was observed that some amount of dye was adsorbed on the surface of the catalyst during this mixing process, and the extent of dye adsorption varied with the composition and nature of the catalyst. To this mixture, 2 mL of 30% H_2O_2 was added, and the reaction mixture was irradiated by simulated solar light emitted from a solar light simulator, which is equipped with a 150 W Xenon lamp. A 3 mL aliquot of the reaction mixture was collected just before the exposure of light, and this point was considered as the starting point (t = 0). The color of the dye solution started to fade because of the exposure to light. The change of the concentration of dye with the progress of the reaction time was monitored spectrophotometrically by using a UV−vis spectrophotometer and following the decrease of intensity of the λ_{max} peak with increasing reaction time (the λ_{max} values of MB, MO, and CR are 664, 463, and 500 nm, respectively).

In the UV−vis spectra, the absorbance of the dye is proportional to its concentration. The ratio of absorbance of dye A_t (measured at time t) to A_0 (measured at t = 0) is equal to C_t/C_0 (where C_t and C_0 are the concentrations of the dye at time t and t = 0, respectively). The % decomposition of the dye because of the photocatalysis reaction was determined from C_t/C_0. The optimal composition of the CF−gC_3N_4 nanocomposite which exhibited the highest catalytic activity was determined by studying the photocatalysis reaction of these model dye solutions. Then, photodegradation reaction was performed for a mixture of dye solution containing 25 ppm MB, 25 ppm CR, and 10 ppm MO, using this catalyst.

The photocatalytic efficiency of the catalyst having optimal composition was also tested for the industrially used dyes (such as Turq CL-B, Yell CL-2R, and Red CL-5B). First, the photodegradation of individual dye solution was performed, followed by a mixture of dye solution (the total concentration

https://dx.doi.org/10.1021/acsomega.0c05809
ACS Omega 2021, 6, 4831−4841

of Turq CL-B, Yell CL-2R, and Red CL-5B in the mixture was 10 ppm).

After the completion of the photocatalysis reaction, the catalyst was recovered from the reaction mixture by a magnetic separation method, where a permanent magnet (N35-grade NdFeB magnet having an energy product BH_{max} = 33−36 MGOe) was used externally. After recovery, the catalyst was washed with ethanol. The absence of any dye in ethanol after washing indicated that all dye molecules present in the reaction mixture along with the dye molecules which were adsorbed on the surface of the catalyst were completely photodegraded. After washing the catalyst, it was dried, and the next cycle of the reaction was performed. The TOC removal ratio of the dye solutions after photocatalysis was calculated by using the following equation[88]

$$\frac{TOC_i - TOC_f}{TOC_i} \quad (10)$$

TOC_i and TOC_f are the TOC contents of the dye solution before and after the photocatalysis reaction.

The details of the chemicals and instruments used in this study are provided in the Supporting Information.

■ ASSOCIATED CONTENT

Supporting Information

The Supporting Information is available free of charge at https://pubs.acs.org/doi/10.1021/acsomega.0c05809.

Details of chemicals, details of instruments, comparison of photocatalytic efficiency of 50CF−50gC_3N_4 with other gC_3N_4-based photocatalysts; XRD patterns of pure $CoFe_2O_4$, pure gC_3N_4, 95CF−5gC_3N_4, 90CF−10gC_3N_4, 85CF−15gC_3N_4, and 75CF−25gC_3N_4; EDS of 50CF−50gC_3N_4; FT-IR spectra of CF, 50CF−50gC_3N_4, and gC_3N_4; Raman spectra of CF, 50CF−50gC_3N_4, and gC_3N_4; TGA curves of pure gC_3N_4, 50CF−50gC_3N_4, 75CF−25gC_3N_4, 85CF−15gC_3N_4, 90CF−10gC_3N_4, 95CF−5gC_3N_4, and pure CF in the temperature range 35−800 °C; UV−vis diffuse absorption spectra of pure gC_3N_4, 50CF−50gC_3N_4, 75CF−25gC_3N_4, 85CF−15gC_3N_4, 90CF−10gC_3N_4, and 95CF−5gC_3N_4; time-dependent UV−vis spectral changes of the photodecomposition reaction and the photodegradation rates of MB, MO, and CR catalyzed by different CF−gC_3N_4 nanocomposites; and XRD plot and FESEM image of the used 50CF−50gC_3N_4 catalyst (PDF)

■ AUTHOR INFORMATION

Corresponding Author

Narendra Nath Ghosh − *Nano-materials Laboratory, Department of Chemistry, Birla Institute of Technology and Science, Zuarinagar, Goa 403726, India;* orcid.org/0000-0002-8338-7292; Phone: +91 832 2580318; Email: naren70@yahoo.com; Fax: +91 832 25570339

Authors

Debika Gogoi − *Nano-materials Laboratory, Department of Chemistry, Birla Institute of Technology and Science, Zuarinagar, Goa 403726, India*

Priyanka Makkar − *Nano-materials Laboratory, Department of Chemistry, Birla Institute of Technology and Science, Zuarinagar, Goa 403726, India*

Complete contact information is available at: https://pubs.acs.org/10.1021/acsomega.0c05809

Notes

The authors declare no competing financial interest.

■ ACKNOWLEDGMENTS

The authors are grateful to the Central Sophisticated Instrumentation Facility (CSIF) of BITS Pilani, K K Birla Goa campus, for providing the FESEM and Raman facilities and also thankful to ABSTCPL, Mumbai and BITS Pilani, for sponsoring the solar light simulator instrument.

■ REFERENCES

(1) Hu, H.; Xin, J. H.; Hu, H.; Wang, X.; Miao, D.; Liu, Y. Synthesis and stabilization of metal nanocatalysts for reduction reactions−a review. *J. Mater. Chem. A* **2015**, *3*, 11157−11182.

(2) Buthelezi, S.; Olaniran, A.; Pillay, B. Textile dye removal from wastewater effluents using bioflocculants produced by indigenous bacterial isolates. *Molecules* **2012**, *17*, 14260−14274.

(3) Aksu, Z. Application of biosorption for the removal of organic pollutants: a review. *Process Biochem.* **2005**, *40*, 997−1026.

(4) Ghosh, B. K.; Ghosh, N. N. Applications of metal nanoparticles as catalysts in cleaning dyes containing industrial effluents: a review. *J. Nanosci. Nanotechnol.* **2018**, *18*, 3735−3758.

(5) Patel, R.; Suresh, S. Decolourization of azo dyes using magnesium-palladium system. *J. Hazard. Mater.* **2006**, *137*, 1729−1741.

(6) Manu, B.; Chaudhari, S. Anaerobic decolorisation of simulated textile wastewater containing azo dyes. *Bioresour. Technol.* **2002**, *82*, 225−231.

(7) Bafana, A.; Devi, S. S.; Chakrabarti, T. Azo dyes: past, present and the future. *Environ. Rev.* **2011**, *19*, 350−371.

(8) Ahmad, A.; Mohd-Setapar, S. H.; Chuong, C. S.; Khatoon, A.; Wani, W. A.; Kumar, R.; Rafatullah, M. Recent advances in new generation dye removal technologies: novel search for approaches to reprocess wastewater. *RSC Adv.* **2015**, *5*, 30801−30818.

(9) Divyapriya, G.; Nambi, I.; Senthilnathan, J. Nanocatalysts in Fenton based advanced oxidation process for water and wastewater treatment. *J. Bionanoscience* **2016**, *10*, 356−368.

(10) Suhas, V. K. G. Application of low-cost adsorbents for dye removal−a review. *J. Environ. Manage.* **2009**, *90*, 2313−2342.

(11) Verma, A. K.; Dash, R. R.; Bhunia, P. A review on chemical coagulation/flocculation technologies for removal of colour from textile wastewaters. *J. Environ. Manage.* **2012**, *93*, 154−168.

(12) Coughlin, M. F.; Kinkle, B. K.; Tepper, A.; Bishop, P. L. Characterization of aerobic azo dye-degrading bacteria and their activity in biofilms. *Water Sci. Technol.* **1997**, *36*, 215−220.

(13) Oturan, M. A.; Aaron, J.-J. Advanced oxidation processes in water/wastewater treatment: principles and applications. A review. *Crit. Rev. Environ. Sci. Technol.* **2014**, *44*, 2577−2641.

(14) Asghar, A.; Raman, A. A. A.; Daud, W. M. A. W. Advanced oxidation processes for in-situ production of hydrogen peroxide/hydroxyl radical for textile wastewater treatment: a review. *J. Clean. Prod.* **2015**, *87*, 826−838.

(15) Robinson, T.; McMullan, G.; Marchant, R.; Nigam, P. Remediation of dyes in textile effluent: a critical review on current treatment technologies with a proposed alternative. *Bioresour. Technol.* **2001**, *77*, 247−255.

(16) Slokar, Y. M.; Majcen Le Marechal, A. Methods of decoloration of textile wastewaters. *Dyes Pigm.* **1998**, *37*, 335−356.

(17) Schneider, J.; Matsuoka, M.; Takeuchi, M.; Zhang, J.; Horiuchi, Y.; Anpo, M.; Bahnemann, D. W. Understanding TiO_2 photocatalysis: mechanisms and materials. *Chem. Rev.* **2014**, *114*, 9919−9986.

(18) Lee, K. M.; Lai, C. W.; Ngai, K. S.; Juan, J. C. Recent developments of zinc oxide based photocatalyst in water treatment technology: a review. *Water Res.* **2016**, *88*, 428−448.

(19) Kumar, S. G.; Devi, L. G. Review on modified TiO_2 photocatalysis under UV/visible light: selected results and related

mechanisms on interfacial charge carrier transfer dynamics. *J. Phys. Chem. A* **2011**, *115*, 13211−13241.
(20) Nakata, K.; Fujishima, A. TiO_2 photocatalysis: Design and applications. *J. Photochem. Photobiol., C* **2012**, *13*, 169−189.
(21) Fujishima, A.; Rao, T. N.; Tryk, D. A. Titanium dioxide photocatalysis. *J. Photochem. Photobiol., C* **2000**, *1*, 1−21.
(22) Fujishima, A.; Zhang, X. Titanium dioxide photocatalysis: present situation and future approaches. *C. R. Chim.* **2006**, *9*, 750−760.
(23) Yang, X.; Chen, W.; Huang, J.; Zhou, Y.; Zhu, Y.; Li, C. Rapid degradation of methylene blue in a novel heterogeneous Fe_3O_4@rGO@TiO_2-catalyzed photo-Fenton system. *Sci. Rep.* **2015**, *5*, 10632.
(24) Liu, Y. Hydrothermal synthesis of TiO_2−RGO composites and their improved photocatalytic activity in visible light. *RSC Adv.* **2014**, *4*, 36040−36045.
(25) Fu, Y.; Wang, X. Magnetically separable $ZnFe_2O_4$−graphene catalyst and its high photocatalytic performance under visible light irradiation. *Ind. Eng. Chem. Res.* **2011**, *50*, 7210−7218.
(26) Leary, R.; Westwood, A. Carbonaceous nanomaterials for the enhancement of TiO_2 photocatalysis. *Carbon* **2011**, *49*, 741−772.
(27) Zhang, F.; Li, Y.-H.; Li, J.-Y.; Tang, Z.-R.; Xu, Y.-J. 3D graphene-based gel photocatalysts for environmental pollutants degradation. *Environ. Pollut.* **2019**, *253*, 365−376.
(28) Weng, B.; Lu, K.-Q.; Tang, Z.; Chen, H. M.; Xu, Y.-J. Stabilizing ultrasmall Au clusters for enhanced photoredox catalysis. *Nat. Commun.* **2018**, *9*, 1543.
(29) Li, Y.-H.; Li, J.-Y.; Xu, Y.-J. Bimetallic Nanoparticles as Cocatalysts for Versatile Photoredox Catalysis. *Energy Chem.* **2020**, *3*, 100047.
(30) Zhang, N.; Yang, M.-Q.; Liu, S.; Sun, Y.; Xu, Y.-J. Waltzing with the versatile platform of graphene to synthesize composite photocatalysts. *Chem. Rev.* **2015**, *115*, 10307−10377.
(31) Han, C.; Li, Y.-H.; Qi, M.-Y.; Zhang, F.; Tang, Z.-R.; Xu, Y.-J. Surface/Interface Engineering of Carbon-Based Materials for Constructing Multidimensional Functional Hybrids. *Sol. RRL* **2020**, *4*, 1900577.
(32) Kumar, S.; T, S.; Kumar, B.; Baruah, A.; Shanker, V. Synthesis of magnetically separable and recyclable g-C_3N_4−Fe_3O_4 hybrid nanocomposites with enhanced photocatalytic performance under visible-light irradiation. *J. Phys. Chem. C* **2013**, *117*, 26135−26143.
(33) Tian, Y.; Chang, B.; Lu, J.; Fu, J.; Xi, F.; Dong, X. Hydrothermal synthesis of graphitic carbon nitride−Bi_2WO_6 heterojunctions with enhanced visible light photocatalytic activities. *ACS Appl. Mater. Interfaces* **2013**, *5*, 7079−7085.
(34) Wang, Y.; Bai, X.; Pan, C.; He, J.; Zhu, Y. Enhancement of photocatalytic activity of Bi_2WO_6hybridized with graphite-like C_3N_4. *J. Mater. Chem.* **2012**, *22*, 11568−11573.
(35) Chen, L.; Ma, W.; Dai, J.; Zhao, J.; Li, C.; Yan, Y. Facile synthesis of highly efficient graphitic-C_3N_4/$ZnFe_2O_4$ heterostructures enhanced visible-light photocatalysis for spiramycin degradation. *J. Photochem. Photobiol., A* **2016**, *328*, 24−32.
(36) Ji, H.; Jing, X.; Xu, Y.; Yan, J.; Li, H.; Li, Y.; Huang, L.; Zhang, Q.; Xu, H.; Li, H. Magnetic g-C_3N_4/$NiFe_2O_4$ hybrids with enhanced photocatalytic activity. *RSC Adv.* **2015**, *5*, 57960−57967.
(37) Yao, Y.; Cai, Y.; Lu, F.; Qin, J.; Wei, F.; Xu, C.; Wang, S. Magnetic $ZnFe_2O_4$-C_3N_4 hybrid for photocatalytic degradation of aqueous organic pollutants by visible light. *Ind. Eng. Chem. Res.* **2014**, *53*, 17294−17302.
(38) Sarkar, S.; Basak, D. One-step nano-engineering of dispersed Ag−ZnO nanoparticles' hybrid in reduced graphene oxide matrix and its superior photocatalytic property. *CrystEngComm* **2013**, *15*, 7606−7614.
(39) Sarkar, S.; Basak, D. The reduction of graphene oxide by zinc powder to produce a zinc oxide-reduced graphene oxide hybrid and its superior photocatalytic activity. *Chem. Phys. Lett.* **2013**, *561*−*562*, 125−130.
(40) Ge, L.; Han, C.; Liu, J. In situ synthesis and enhanced visible light photocatalytic activities of novel PANI−gC_3N_4 composite photocatalysts. *J. Mater. Chem.* **2012**, *22*, 11843−11850.
(41) Hassani, A.; Eghbali, P.; Ekicibil, A.; Metin, Ö. Monodisperse cobalt ferrite nanoparticles assembled on mesoporous graphitic carbon nitride ($CoFe_2O_4$/mpg-C_3N_4): a magnetically recoverable nanocomposite for the photocatalytic degradation of organic dyes. *J. Magn. Magn Mater.* **2018**, *456*, 400−412.
(42) Zhang, S.; Li, J.; Zeng, M.; Zhao, G.; Xu, J.; Hu, W.; Wang, X. In situ synthesis of water-soluble magnetic graphitic carbon nitride photocatalyst and its synergistic catalytic performance. *ACS Appl. Mater. Interfaces* **2013**, *5*, 12735−12743.
(43) Sun, J.-X.; Yuan, Y.-P.; Qiu, L.-G.; Jiang, X.; Xie, A.-J.; Shen, Y.-H.; Zhu, J.-F. Fabrication of composite photocatalyst gC_3N_4-ZnO and enhancement of photocatalytic activity under visible light. *Dalton Trans.* **2012**, *41*, 6756−6763.
(44) Alcudia-Ramos, M. A.; Fuentez-Torres, M. O.; Ortiz-Chi, F.; Espinosa-González, C. G.; Hernández-Como, N.; García-Zaleta, D. S.; Kesarla, M. K.; Torres-Torres, J. G.; Collins-Martínez, V.; Godavarthi, S. Fabrication of g-C_3N_4/TiO_2 heterojunction composite for enhanced photocatalytic hydrogen production. *Ceram. Int.* **2020**, *46*, 38−45.
(45) Shen, H.; Zhao, X.; Duan, L.; Liu, R.; Li, H. Enhanced visible light photocatalytic activity in SnO_2@g-C_3N_4 core-shell structures. *Mater. Sci. Eng., B* **2017**, *218*, 23−30.
(46) Huang, L.; Xu, H.; Li, Y.; Li, H.; Cheng, X.; Xia, J.; Xu, Y.; Cai, G. Visible-light-induced WO_3/gC_3N_4 composites with enhanced photocatalytic activity. *Dalton Trans.* **2013**, *42*, 8606−8616.
(47) Gan, L.; Shang, S.; Yuen, C. W. M.; Jiang, S.-x.; Hu, E. Hydrothermal synthesis of magnetic $CoFe_2O_4$/graphene nanocomposites with improved photocatalytic activity. *Appl. Surf. Sci.* **2015**, *351*, 140−147.
(48) Moitra, D.; Chandel, M.; Ghosh, B. K.; Jani, R. K.; Patra, M. K.; Vadera, S. R.; Ghosh, N. N. A simple 'in situ'co-precipitation method for the preparation of multifunctional $CoFe_2O_4$−reduced graphene oxide nanocomposites: excellent microwave absorber and highly efficient magnetically separable recyclable photocatalyst for dye degradation. *RSC Adv.* **2016**, *6*, 76759−76772.
(49) Huang, S.; Xu, Y.; Xie, M.; Xu, H.; He, M.; Xia, J.; Huang, L.; Li, H. Synthesis of magnetic $CoFe_2O_4$/g-C_3N_4 composite and its enhancement of photocatalytic ability under visible-light. *Colloids Surf., A* **2015**, *478*, 71−80.
(50) Lu, H. M.; Zheng, W. T.; Jiang, Q. Saturation magnetization of ferromagnetic and ferrimagnetic nanocrystals at room temperature. *J. Phys. D: Appl. Phys.* **2007**, *40*, 320.
(51) Hassani, A.; Eghbali, P.; Metin, Ö. Sonocatalytic removal of methylene blue from water solution by cobalt ferrite/mesoporous graphitic carbon nitride ($CoFe_2O_4$/mpg-C_3N_4) nanocomposites: response surface methodology approach. *Environ. Sci. Pollut. Res.* **2018**, *25*, 32140−32155.
(52) Inbaraj, D. J.; Chandran, B.; Mangalaraj, C. Synthesis of $CoFe_2O_4$ and $CoFe_2O_4$/g-C_3N_4 nanocomposite via honey mediated sol-gel auto combustion method and hydrothermal method with enhanced photocatalytic and efficient Pb^{+2} adsorption property. *Mater. Res. Express* **2019**, *6*, 055501.
(53) Yao, Y.; Wu, G.; Lu, F.; Wang, S.; Hu, Y.; Zhang, J.; Huang, W.; Wei, F. Enhanced photo-Fenton-like process over Z-scheme $CoFe_2O_4$/gC_3N_4 heterostructures under natural indoor light. *Environ. Sci. Pollut. Res.* **2016**, *23*, 21833−21845.
(54) Deng, J.; Shao, Y.; Gao, N.; Tan, C.; Zhou, S.; Hu, X. $CoFe_2O_4$ magnetic nanoparticles as a highly active heterogeneous catalyst of oxone for the degradation of diclofenac in water. *J. Hazard. Mater.* **2013**, *262*, 836−844.
(55) Dong, F.; Sun, Y.; Wu, L.; Fu, M.; Wu, Z. Facile transformation of low cost thiourea into nitrogen-rich graphitic carbon nitride nanocatalyst with high visible light photocatalytic performance. *Catal. Sci. Technol.* **2012**, *2*, 1332−1335.
(56) Xu, J.; Wang, Y.; Zhu, Y. Nanoporous graphitic carbon nitride with enhanced photocatalytic performance. *Langmuir* **2013**, *29*, 10566−10572.
(57) Xu, H.; Yan, J.; Xu, Y.; Song, Y.; Li, H.; Xia, J.; Huang, C.; Wan, H. Novel visible-light-driven AgX/graphite-like C_3N_4 (X=Br, I)

https://dx.doi.org/10.1021/acsomega.0c05809
ACS Omega 2021, 6, 4831−4841

hybrid materials with synergistic photocatalytic activity. *Appl. Catal., B* **2013**, *129*, 182−193.
(58) Di, J.; Xia, J.; Yin, S.; Xu, H.; He, M.; Li, H.; Xu, L.; Jiang, Y. A gC_3N_4/BiOBr visible-light-driven composite: synthesis via a reactable ionic liquid and improved photocatalytic activity. *RSC Adv.* **2013**, *3*, 19624−19631.
(59) Xu, Y.; Xu, H.; Yan, J.; Li, H.; Huang, L.; Xia, J.; Yin, S.; Shu, H. A plasmonic photocatalyst of Ag/AgBr nanoparticles coupled with g-C_3N_4 with enhanced visible-light photocatalytic ability. *Colloids Surf., A* **2013**, *436*, 474−483.
(60) Khabashesku, V. N.; Zimmerman, J. L.; Margrave, J. L. Powder synthesis and characterization of amorphous carbon nitride. *Chem. Mater.* **2000**, *12*, 3264−3270.
(61) Wu, S.; Wen, S.; Xu, X.; Huang, G.; Cui, Y.; Li, J.; Qu, A. Facile synthesis of porous graphene-like carbon nitride nanosheets with high surface area and enhanced photocatalytic activity via one-step catalyst-free solution self-polymerization. *Appl. Surf. Sci.* **2018**, *436*, 424−432.
(62) Niu, P.; Zhang, L.; Liu, G.; Cheng, H.-M. Graphene-like carbon nitride nanosheets for improved photocatalytic activities. *Adv. Funct. Mater.* **2012**, *22*, 4763−4770.
(63) Fu, M.; Jiao, Q.; Zhao, Y.; Li, H. Vapor diffusion synthesis of $CoFe_2O_4$ hollow sphere/graphene composites as absorbing materials. *J. Mater. Chem. A* **2014**, *2*, 735−744.
(64) Wang, H.; Zhang, X.; Xie, J.; Zhang, J.; Ma, P.; Pan, B.; Xie, Y. Structural distortion in graphitic-C_3N_4 realizing an efficient photoreactivity. *Nanoscale* **2015**, *7*, 5152−5156.
(65) Wang, Y.; Yang, W.; Chen, X.; Wang, J.; Zhu, Y. Photocatalytic activity enhancement of core-shell structure g-C_3N_4@TiO_2 via controlled ultrathin g-C_3N_4 layer. *Appl. Catal., B* **2018**, *220*, 337−347.
(66) Shiraishi, Y.; Kanazawa, S.; Sugano, Y.; Tsukamoto, D.; Sakamoto, H.; Ichikawa, S.; Hirai, T. Highly selective production of hydrogen peroxide on graphitic carbon nitride (g-C_3N_4) photocatalyst activated by visible light. *ACS Catal.* **2014**, *4*, 774−780.
(67) Wen, J.; Xie, J.; Chen, X.; Li, X. A review on g-C_3N_4-based photocatalysts. *Appl. Surf. Sci.* **2017**, *391*, 72−123.
(68) Xiang, Q.; Yu, J.; Jaroniec, M. Preparation and enhanced visible-light photocatalytic H_2-production activity of graphene/C_3N_4 composites. *J. Phys. Chem. C* **2011**, *115*, 7355−7363.
(69) Mariosi, F. R.; Venturini, J.; da Cas Viegas, A.; Bergmann, C. P. Lanthanum-doped spinel cobalt ferrite ($CoFe_2O_4$) nanoparticles for environmental applications. *Ceram. Int.* **2020**, *46*, 2772−2779.
(70) Wang, X.; Wang, A.; Ma, J. Visible-light-driven photocatalytic removal of antibiotics by newly designed C_3N_4@$MnFe_2O_4$-graphene nanocomposites. *J. Hazard. Mater.* **2017**, *336*, 81−92.
(71) Vignesh, K.; Suganthi, A.; Min, B.-K.; Kang, M. Photocatalytic activity of magnetically recoverable $MnFe_2O_4$/g-C_3N_4/TiO_2 nanocomposite under simulated solar light irradiation. *J. Mol. Catal. A: Chem.* **2014**, *395*, 373−383.
(72) Kubelka, P.; Munk, F. An article on optics of paint layers. *Z. Tech. Phys.* **1931**, *12*, 259−274.
(73) Xu, Q.; Zhang, L.; Cheng, B.; Fan, J.; Yu, J. S-scheme heterojunction photocatalyst. *Chem* **2020**, *6*, 1543−1559.
(74) Xia, P.; Cao, S.; Zhu, B.; Liu, M.; Shi, M.; Yu, J.; Zhang, Y. Designing a 0D/2D S-Scheme Heterojunction over Polymeric Carbon Nitride for Visible-Light Photocatalytic Inactivation of Bacteria. *Angew. Chem., Int. Ed.* **2020**, *59*, 5218−5225.
(75) Xie, Q.; He, W.; Liu, S.; Li, C.; Zhang, J.; Wong, P. K. Bifunctional S-scheme g-C_3N_4/Bi/$BiVO_4$ hybrid photocatalysts toward artificial carbon cycling. *Chin. J. Catal.* **2020**, *41*, 140−153.
(76) Xu, F.; Meng, K.; Cheng, B.; Wang, S.; Xu, J.; Yu, J. Unique S-scheme heterojunctions in self-assembled TiO_2/$CsPbBr_3$ hybrids for CO_2 photoreduction. *Nat. Commun.* **2020**, *11*, 1−9.
(77) Qin, D.; Xia, Y.; Li, Q.; Yang, C.; Qin, Y.; Lv, K. One-pot calcination synthesis of $Cd_{0.5}Zn_{0.5}S$/g-C_3N_4 photocatalyst with a step-scheme heterojunction structure. *J. Mater. Sci. Technol.* **2020**, *56*, 206−215.
(78) Guo, X.; Ai, S.; Yang, D.; Zhao, L.; Ding, H. Synergistic photocatalytic and Fenton-like degradation of organic contaminants using peroxymonosulfate activated by $CoFe_2O_4$@g-C_3N_4 composite. *Environ. Technol.* **2019**, 1−14.
(79) Xian, T.; Yang, H.; Di, L. J.; Dai, J. F. Enhanced photocatalytic activity of $BaTiO_3$@g-C_3N_4 for the degradation of methyl orange under simulated sunlight irradiation. *J. Alloys Compd.* **2015**, *622*, 1098−1104.
(80) Tian, Y.; Cheng, F.; Zhang, X.; Yan, F.; Zhou, B.; Chen, Z.; Liu, J.; Xi, F.; Dong, X. Solvothermal synthesis and enhanced visible light photocatalytic activity of novel graphitic carbon nitride−Bi_2MoO_6 heterojunctions. *Powder Technol.* **2014**, *267*, 126−133.
(81) Zhu, Z.; Wang, Z.; Di, J.; Long, Y.; Li, W. Enhanced visible-light photocatalytic properties of g-C_3N_4 by coupling with $ZnAl_2O_4$. *Catal. Commun.* **2016**, *86*, 86−90.
(82) Tian, Y.; Chang, B.; Yang, Z.; Zhou, B.; Xi, F.; Dong, X. Graphitic carbon nitride−$BiVO_4$ heterojunctions: simple hydrothermal synthesis and high photocatalytic performances. *RSC Adv.* **2014**, *4*, 4187−4193.
(83) Wang, Y.; Wang, Z.; Muhammad, S.; He, J. Graphite-like C_3N_4 hybridized $ZnWO_4$ nanorods: Synthesis and its enhanced photocatalysis in visible light. *CrystEngComm* **2012**, *14*, 5065−5070.
(84) Yu, Q.; Guo, S.; Li, X.; Zhang, M. Template free fabrication of porous g-C3N4/graphene hybrid with enhanced photocatalytic capability under visible light. *Mater. Technol.* **2014**, *29*, 172−178.
(85) Alenizi, M. A.; Kumar, R.; Aslam, M.; Alseroury, F.; Barakat, M. Construction of a ternary gC_3N_4/TiO_2@polyaniline nanocomposite for the enhanced photocatalytic activity under solar light. *Sci. Rep.* **2019**, *9*, 12091.
(86) Li, C.; Sun, Z.; Li, X.; Liu, L.; Zheng, S. Facile fabrication of g-C_3N_4/precipitated silica composite with enhanced visible-light photoactivity for the degradation of rhodamine B and Congo red. *Adv. Powder Technol.* **2016**, *27*, 2051−2060.
(87) Tu, D.; Liao, H.; Deng, Q. Synthesis of BN/g-C_3N_4 as Visible-light-driven Photocatalysts for Degradation of Different Organic Pollutants. *ChemistrySelect* **2018**, *3*, 7170−7177.
(88) Hu, C.; Wang, M.-S.; Chen, C.-H.; Chen, Y.-R.; Huang, P.-H.; Tung, K.-L. Phosphorus-doped g-C_3N_4 integrated photocatalytic membrane reactor for wastewater treatment. *J. Membr. Sci.* **2019**, *580*, 1−11.

https://dx.doi.org/10.1021/acsomega.0c05809
ACS Omega 2021, 6, 4831−4841